The effect of confinement on the stability of viscous planar jets and wakes

S. J. R E E S AND M. P. J U N I P E R†

Department of Engineering, University of Cambridge, Trumpington Street, Cambridge CB2 1PZ, UK

This theoretical study examines confined viscous planar jet/wake flows with continuous velocity profiles. These flows are characterized by the shear, confinement, Reynolds number and shear-layer thickness. The primary aim of this paper is to determine the effect of confinement on viscous jets and wakes and to compare these results with corresponding inviscid results. The secondary aim is to consider the effect of viscosity and shear-layer thickness. A spatio-temporal analysis is performed in order to determine absolute/convective instability criteria. This analysis is carried out numerically by solving the Orr–Sommerfeld equation using a Chebyshev collocation method. Results are produced over a large range of parameter space, including both co-flow and counter-flow domains and confinements corresponding to $0.1 < h_2/h_1 < 10$, where the subscripts 1 and 2 refer to the inner and outer streams, respectively. The Reynolds number, which is defined using the channel width, takes values between 10 and 1000. Different velocity profiles are used so that the shear layers occupy between 1/2 and 1/24 of the channel width. Results indicate that confinement has a destabilizing effect on both inviscid and viscous flows. Viscosity is found always to be stabilizing, although its effect can safely be neglected above $Re = 1000$. Thick shear layers are found to have a stabilizing effect on the flow, but infinitely thin shear layers are not the most unstable; having shear layers of a small, but finite, thickness gives rise to the strongest instability.

1. Introduction

This paper describes the effect of confinement on the local stability of planar viscous jets and wakes. The model (figure 1) consists of a uniform viscous fluid confined between two flat plates. The fluid moves parallel to the plates and has a smooth velocity profile with two inflexion points. The profile is symmetric about the centreline and had no streamwise variation. If the inner part of the fluid moves faster than the outer parts, it models a jet flow. If the outer parts of the fluid move faster than the inner part, it models a wake flow. In order to avoid having to include boundary layers, the walls are given the same velocity as the outer fluid.

This paper focuses on the transition from local convective to local absolute instability. This is a necessary (but not sufficient) condition for the existence of self-sustained global instabilities, which are observed in numerical simulations or experiments. The connection between local and global instability was studied by Chomaz, Huerre & Redekopp (1988) for the Ginzburg–Landau equation and by Monkewitz (1988) for a planar model of the wake flow behind a cylinder. Monkewitz

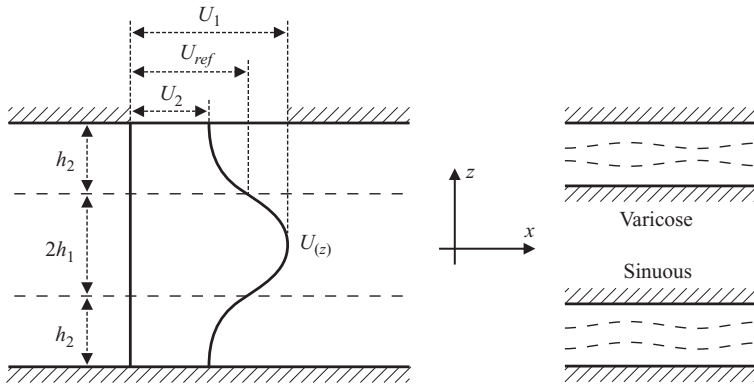† Email address for correspondence: mpj1001@cam.ac.uk

FIGURE 1. Model base flow.

(1988) showed that the sequence of transitions behind a cylinder wake as the Reynolds number is increased confirms the scenario described by Chomaz *et al.* (1988): transition from stability to convective instability, transition from convective to local absolute instability and finally transition to a self-sustained global mode, via a Hopf bifurcation, when a sufficiently large portion of the flow has become absolutely unstable. This complemented the experimental work of Mathis, Provansal & Boyer (1984), who had shown that the onset of the global oscillations in a planar cylinder wake is via a Hopf bifurcation to a global mode, and the theoretical work of Koch (1985), who had shown that planar wakes in a uniform fluid contain an absolutely unstable region. For these shear flows, Delbende & Chomaz (1998) showed that the velocities of the front and back of an impulse response wavepacket are determined by the linear instability properties, while the saturated amplitude in the centre of the wavepacket is determined by the nonlinear properties. Put together, these studies justify the use of the transition from local convective to local absolute linear instability as a proxy for the transition from a globally stable to a globally unstable flow. Furthermore, the global stability properties can be predicted remarkably well from the local stability properties. This works for linear global modes (Huerre & Monkewitz 1990) and for nonlinear global modes (Pier 2002).

Unconfined jets and wakes have been extensively studied. For instance, in their theoretical spatio-temporal stability analysis of planar jets and wakes with non-uniform density ratios, Yu & Monkewitz (1990) showed that unconfined planar jets and wakes can be absolutely unstable even in co-flow. They showed that this is due to the interaction between the two shear layers, and not due to the shear layers themselves, which can only be independently absolutely unstable in counter-flow. In an experimental study of planar jets, Yu & Monkewitz (1993) showed that hot jets, which contain absolutely unstable regions, exhibit self-excited global oscillations while cold jets, which do not contain absolutely unstable regions, do not exhibit self-excited global oscillations. As for the studies of planar wakes described in the previous paragraph, the onset of these global oscillations was identified as a Hopf bifurcation. The same has been found in round low density jets, both theoretically (Monkewitz & Sohn 1988) and experimentally (Sreenivasan, Raghu & Kyle 1989).

Confined jets and wakes have received less attention. Theoretical studies, summarized shortly, have dealt with both jets and wakes. In these studies, confinement is quantified by the ratio of the outer flow thickness, h_2, to the inner flow half-thickness, h_1, which is given the symbol $h \equiv h_2/h_1$. These theoretical studies predict

that confined wakes have more interesting instability behaviour than confined jets. It is not surprising, therefore, that all experimental and numerical studies relevant to this paper have focused on confined wakes rather than confined jets. In these studies, which are on confined circular, square, rectangular and triangular cylinders, confinement is quantified by the ratio of the cylinder diameter to the duct width, which is called the blockage ratio and given the symbol β. This is related to h by $h = 1/\beta - 1$.

At high Reynolds number, confinement destabilizes wake flows. This is seen particularly clearly in the experimental study of Richter & Naudascher (1976), who examined the fluctuating forces on a confined circular cylinder at $10^4 < Re < 10^6$. The fluctuating cross-stream force, which arises from sinuous vortex shedding, increased markedly as the flow was confined, becoming eight times greater than the unconfined case when the cylinder's diameter was half the distance between the plates ($h = 1$, $\beta = 0.5$). The same effect was observed by Kim, Yang & Senda (2004) in their numerical study of a confined square cylinder at $Re = 3000$ and one value of confinement, $h = 4$. The fluctuating cross-stream force was 1.79 times greater in their confined case than in the corresponding unconfined case. (The advantage of a square cylinder is that, unlike a round cylinder, any effects due to the shifting of the separation points can be ruled out.) A similar effect is found in the high-Reynolds-number flow around a cylinder that is placed next to a wall. Bearman & Zdravkovich (1978) found, at $Re = 45\,000$, that the vortex shedding frequency became better-defined as their circular cylinder approached the wall. Similarly, Hwang & Yao (1997) found, at $Re = 1000$ and $h = 5.5, 3.5, 1.5$, that the fluctuating cross-stream force increased as their square cylinder approached the wall. Both studies suggest that this semi-confined configuration, like the fully confined configuration, has a stronger global mode than the unconfined case.

For inviscid planar jets and wakes, the theoretical analysis of Juniper (2006) explained the strong destabilizing effect of confinement around $h = 1$ in terms of the interaction between modes with zero group velocity in the inner flow and outer flows. The jet/wake flow is particularly unstable when these modes, which correspond to saddle points in the wavenumber plane, have similar cross-stream wavenumbers. For the sinuous motion of uniform density planar wakes, this occurs around $h = 1$, which would explain the strong cross-stream force fluctuations and well-defined spectral peaks in the studies reported in the previous paragraph. Although this paper is concerned with planar jets and wakes, it is worth mentioning that the same effect is found in round jets and wakes (Juniper 2008). It is particularly strong for the $m = 1$ helical mode of confined dense wakes around $h = 0.8$. This is exploited in the design of fuel injectors in rocket engines, for example in the Space Shuttle Main Engine and in the Vulcan engine of Ariane V, in order to generate good mixing in the combustion chamber (Juniper & Candel 2003).

For viscous planar jets and wakes, the relative influence of viscosity is determined by the Reynolds number, which is defined with reference either to the width of the jet/wake or to the width of the duct. These two definitions are related by a factor h. As h is varied, only one Reynolds number can be kept constant, and this choice dictates whether confinement seems to have a stabilizing or a destabilizing effect. A good illustration of this is given by studies of the critical Reynolds number for the onset of oscillations in the wake behind a confined circular cylinder. If the Reynolds number is defined by the width of the object, as in the experimental study of Shair *et al.* (1963), then the critical Reynolds number increases as the flow becomes more confined and hence confinement seems to stabilize the flow. If, however, the Reynolds

number is defined by the width of the duct, as in the numerical study of Chen, Pritchard & Tavener (1995), then the critical Reynolds number decreases as the flow becomes more confined and hence confinement seems to destabilize the flow. Another example is found in the numerical results of Davis, Moore & Purtell (1983) for the fluctuating lift coefficient on a square cylinder in a duct. If the Reynolds number is based on the width of the square then, at given Reynolds number, the r.m.s. cross-stream fluctuations decrease as the flow becomes more confined, hence confinement seems to stabilize the flow. If, however, the results are re-scaled so that the Reynolds number is based on the width of the duct then, at given Reynolds number, the r.m.s. cross-stream fluctuations increase as the flow becomes more confined, hence confinement seems to destabilize the flow. Similar results can be found in Turki, Abbasi & Nasrallah (2003) for a confined square cylinder and De & Dalal (2007) for a confined triangular cylinder. Above a Reynolds number of $Re \approx 750$, Davis *et al.* (1983) found that confinement is destabilizing, regardless of how the Reynolds number is defined, indicating that viscous effects are no longer influential.

The viscosity is uniform in this study, which rules out the two instability mechanisms found by Yih (1967) at long wavelength and Hooper & Boyd (1983) at short wavelength and which are described further by Hinch (1984). Nevertheless, it is interesting to note that Yih's flow, in which two fluids of differing viscosities were confined between flat plates, is most unstable when both fluids have the same width, corresponding to $h = 1$. This suggests that confinement makes a flow more unstable whether the driving mechanism is due to viscosity stratification or due to inertia.

As well as affecting the linear stability of a given base flow, confinement also affects the nonlinear development of such flows. Although this paper is restricted to the linear regime, it is worth mentioning two examples of nonlinear effects. In their numerical study of the flow behind a confined square cylinder at $100 < Re < 1850$, Davis *et al.* (1983) found that vortices appeared along the confining walls as well as in a street behind the cylinder. For the same configuration, but at lower Reynolds number, Camarri & Giannetti (2007) did not find these wall vortices but did find that the von Kármán vortices swapped sides some way down the channel. By varying the inlet velocity profile in their numerical simulations, they were able to show that this is due to the vorticity contained within the inlet Poiseuille profile, rather than an effect of confinement by itself. In this paper, all vorticity is contained within the shear layers of the jet/wake flows in order to avoid boundary layer effects.

The first aim of this paper is to catalogue the effect of confinement on the local instability properties of simple viscous jets and wakes and to compare these with previous studies on inviscid jets and wakes. Qualitatively, the flows that are studied here share the same simple velocity profile. Quantitatively, they are characterized by the confinement, shear, shear-layer thickness and Reynolds number. When combined with the previous papers, this provides a sound physical understanding of the effect of confinement on the local stability properties of jets and wakes. While this paper relates to local stability, the experimental results described earlier relate to global instability. For a thorough comparison with these experimental results, a global stability analysis will be required on a spatially evolving base flow. The second aim of this paper is to examine the effect of the Reynolds number on confined flows to determine the valid range of inviscid models. The third aim of this paper is to examine the influence of the shear-layer profile to determine whether a piecewise linear profile can capture the instability behaviour or whether the exact profile is required.

In §2, the model is presented, the governing equations are derived and a choice of mean velocity is explained. In §3, the local spatio-temporal analysis used throughout

this paper is introduced and the procedure for locating absolutely unstable regions is described. In §4, the effect of varying shear-layer thickness on regions of absolute instability is investigated as a function of shear and confinement. In §5, viscosity is introduced and a similar investigation is carried out looking at the effect of varying the Reynolds number on regions of absolute instability also as a function of shear and confinement. In §6, the effect of confinement on viscous flows is evaluated and a threshold above which viscosity can be ignored is established.

2. Theoretical framework

In this section, the governing equations of the perturbed base flow are derived in the manner of Drazin & Reid (1981). The numerical method for solving this system of equations is outlined and a versatile base flow function is constructed in order to cover the full range of parameter space under investigation.

2.1. *Derivation of the governing equations*

The model consists of a two-dimensional base flow in a confined channel, given by $\boldsymbol{U}^* = (U^*(x^*, z^*), 0, W^*(x^*, z^*))$, where the asterisk denotes dimensional quantities. The channel has infinite extent in the x-direction and confining walls in the z-direction at $z^* = \pm (h_1 + h_2)$. The fluid has uniform density ρ, viscosity μ, and is assumed to be incompressible. No body forces are considered and so gravitational effects are ignored. A parallel flow assumption is made so that the base flow satisfies the conditions

$$U^*(x^*, z^*) \gg W^*(x^*, z^*) \qquad \text{and} \qquad \frac{\partial U^*}{\partial x^*} \ll \frac{U_{max}}{L}, \qquad (2.1)$$

where $U_{max} = \max(U_1, U_2)$ and $L = h_1 + h_2$. For the purpose of this study, the base flow is assumed to be $\boldsymbol{U}^* = (U^*(z^*), 0, 0)$, where U^* takes extremal values U_1 at the centreline, $z^* = 0$, and U_2 at both the walls, $z^* = \pm (h_1 + h_2)$. The average velocity $(U_1 + U_2)/2$ is achieved at $z = \pm h_1$, which marks the boundaries between the inner and outer sections of the flow. Its location is varied in order to change the relative widths of the inner and outer flows and therefore the confinement.

It is convenient at this point to work in a non-dimensional framework. This introduces the following reference scales: velocity, $U_{ref} = (U_1 + U_2)/2$, length $L_{ref} = h_1 + h_2$ and density $\rho_{ref} = \rho$. The dimensionless parameters that characterize the flow are defined: the relative velocity difference, $\Lambda \equiv (U_1 - U_2)/(U_1 + U_2)$; the confinement, given by the relative difference in thickness of the inner and outer streams, $h \equiv (h_2 - h_1)/(h_2 + h_1)$ and the Reynold's number, $Re \equiv U_{ref} L_{ref}/\nu$. The flow properties are then non-dimensionalized (unstarred) in the following manner: $t = t^* U_{ref}/L_{ref}$, $\boldsymbol{x} = \boldsymbol{x}^*/L_{ref}$, $\boldsymbol{U} = \boldsymbol{U}^*/U_{ref}$ and $P = P^*/\rho_{ref} U_{ref}^2$. The cross-stream domain becomes normalized to $z \in [-1 \ 1]$ with the inner–outer flow boundaries occurring at $z = \pm (1 - h)/2$.

The flow is governed by the Navier–Stokes equation along with the incompressibility condition:

$$\left(\frac{\partial \boldsymbol{U}}{\partial t} + \boldsymbol{U} \cdot \nabla \boldsymbol{U} \right) = -\nabla P + \frac{1}{Re} \nabla^2 \boldsymbol{U}, \qquad (2.2)$$

$$\nabla \cdot \boldsymbol{U} = 0. \qquad (2.3)$$

The equations of motion are linearized about this base flow and a normal-mode decomposition is assumed of the form

$$\hat{\boldsymbol{u}} = (\tilde{u}(z), \tilde{v}(z), \tilde{w}(z)) e^{\mathrm{i}(k_x x + k_y y - \omega t)} \qquad \text{and} \qquad \hat{p} = \tilde{p}(z) e^{\mathrm{i}(k_x x + k_y y - \omega t)}. \qquad (2.4)$$

The perturbed three-dimensional system is governed by the equations

$$\left\{\frac{1}{Re}\left(\frac{d^2}{dz^2} - k_x^2 - k_y^2\right) - i(U - c)\right\}\tilde{u} = ik_x\tilde{p} + \frac{dU}{dz}\tilde{w}, \tag{2.5}$$

$$\left\{\frac{1}{Re}\left(\frac{d^2}{dz^2} - k_x^2 - k_y^2\right) - i(U - c)\right\}\tilde{v} = ik_y\tilde{p}, \tag{2.6}$$

$$\left\{\frac{1}{Re}\left(\frac{d^2}{dz^2} - k_x^2 - k_y^2\right) - i(U - c)\right\}\tilde{w} = i\frac{d\tilde{p}}{dz}, \tag{2.7}$$

$$ik_x\tilde{u} + ik_y\tilde{v} + \frac{d\tilde{w}}{dz} = 0, \tag{2.8}$$

along with the boundary conditions

$$\tilde{u} = \tilde{v} = \tilde{w} = 0 \quad \text{at} \quad z = \pm 1. \tag{2.9}$$

Making use of Squire's theorem, it is sufficient to consider two-dimensional perturbations in order to obtain the strongest instability in the long time limit. This can be seen by using the set of transformations

$$k = (k_x^2 + k_y^2)^{1/2}, \quad c = \tilde{c}, \quad ku = k_x\tilde{u} + k_y\tilde{v}, \quad w = \tilde{w} \quad \text{and} \quad p/k = \tilde{p}/k_x. \tag{2.10}$$

This transformation is equivalent to considering the two-dimensional perturbation

$$\hat{u} = (u(z), 0, w(z))e^{i(kx-\omega t)} \quad \text{and} \quad \hat{p} = p(z)e^{i(kx-\omega t)}. \tag{2.11}$$

The three-dimensional system reduces to a two-dimensional system governed by the equations

$$\left\{\frac{1}{Re}\frac{d^2}{dz^2} - k^2 - i(U - c)\right\}u = ikp + \frac{dU}{dz}w, \tag{2.12}$$

$$\left\{\frac{1}{Re}\frac{d^2}{dz^2} - k^2 - i(U - c)\right\}w = i\frac{dp}{dz}, \tag{2.13}$$

$$iku + \frac{dw}{dz} = 0, \tag{2.14}$$

along with the boundary conditions

$$u = w = 0 \quad \text{at} \quad z = \pm 1. \tag{2.15}$$

These boundary conditions are appropriate for this situation, in which the walls move at the same velocity as the outer fluid, so that the combined base flow plus the perturbation obeys the no-slip boundary condition. Because the perturbation is two-dimensional it can be further expressed in terms of a streamfunction, $\psi(x, z, t) = \varphi(z)\exp(i(kx - \omega t))$, hence $u = d\varphi/dz$ and $w = -ik\varphi$. Substituting these expressions into the above equations and eliminating in favour of φ, so as to give a single ordinary differential equation (ODE), yields the Orr–Sommerfeld equation

$$(U - c)\left(\frac{d^2}{dz^2} - k^2\right)\varphi - \frac{d^2U}{dz^2}\varphi + \frac{i}{kRe}\left(\frac{d^4}{dz^4} - 2k^2\frac{d^2}{dz^2} + k^4\right)\varphi = 0, \tag{2.16}$$

along with the boundary conditions

$$k\varphi = \frac{d\varphi}{dz} = 0 \quad \text{at} \quad z = \pm 1. \tag{2.17}$$

2.2. *Numerical method*

The resulting equation is solved using a pseudospectral Chebyshev collocation method, the details of which can be found in Appendix A. Under this numerical discretization, the differential operators become differentiation matrices and the base flow quantities are discretized by their values at the collocation points, z_i:

$$\frac{\mathrm{d}^m}{\mathrm{d}z^m} \to D_{ij}^{(m)} \equiv \boldsymbol{D}^{(m)}, \quad U(z) \to U(z_i)\delta_{ij} \equiv \boldsymbol{U}, \quad \frac{\mathrm{d}^2 U}{\mathrm{d}z^2}(z) \to U''(z_i)\delta_{ij} \equiv \boldsymbol{U}''. \quad (2.18)$$

Following the boundary conditions (2.17), both the Dirichlet, $\varphi = 0$, and Von Neumann, $\mathrm{d}\varphi/\mathrm{d}z = 0$, boundary conditions are built into the basis functions used to construct the differentiation matrices and so are automatically satisfied by the eigenfunction, $\varphi(z)$; see Appendix B.

Implementing this numerical scheme, the Orr–Sommerfeld equation can be rearranged into the form of a generalized eigenvalue problem

$$\boldsymbol{A}\varphi = \omega\boldsymbol{B}\varphi, \quad (2.19)$$

aimed at solving for the wave frequency, ω, given the wavenumber k. This eigenvalue pairing, (k, ω), represents the dispersion relation for the flow. The matrices A_{ij} and B_{ij} are given by

$$\boldsymbol{A} = k\boldsymbol{U}(\boldsymbol{D}^{(2)} - k^2\boldsymbol{I}) - k\boldsymbol{U}'' + \frac{\mathrm{i}}{Re}(\boldsymbol{D}^{(4)} - 2k^2\boldsymbol{D}^{(2)} + k^4\boldsymbol{I}), \quad (2.20)$$

$$\boldsymbol{B} = \boldsymbol{D}^{(2)} - k^2\boldsymbol{I}. \quad (2.21)$$

This can be solved using `MATLAB`'s generalized eigenvalue problem solver `eig`.

2.3. *Saddle points*

This study is interested in the stability properties in the long time limit, which are dominated by modes with zero group velocity. These correspond to eigenvalue pairings, (k, ω), which also satisfy the further property that $\partial\omega/\partial k = 0$. These are saddle points, denoted by the superscripts (k^s, ω^s). Saddle points can be located using an explicit form for $\partial\omega/\partial k$. This is obtained using a differential form of the generalized eigenvalue problem when expressed as

$$\det(\boldsymbol{A} - \omega\boldsymbol{B}) = 0. \quad (2.22)$$

This is given by

$$\frac{\partial\omega}{\partial k} = \frac{\mathrm{tr}\left(\mathrm{adj}(\boldsymbol{A} - \omega\boldsymbol{B})\left(\dfrac{\partial\boldsymbol{A}}{\partial k} - \omega\dfrac{\partial\boldsymbol{B}}{\partial k}\right)\right)}{\mathrm{tr}(\mathrm{adj}\,(\boldsymbol{A} - \omega\boldsymbol{B})\boldsymbol{B})}, \quad (2.23)$$

where tr indicates the trace of the matrix and adj indicates the adjugate of the matrix.

The partial derivatives in (2.23) are easily calculated from (2.20) and (2.21) and are given by

$$\frac{\partial\boldsymbol{A}}{\partial k} = \boldsymbol{U}\left(\boldsymbol{D}^{(2)} - 3k^2\boldsymbol{I}\right) - \boldsymbol{U}'' - \frac{\mathrm{i}}{Re}\left(4k\boldsymbol{D}^{(2)} - 4k^3\boldsymbol{I}\right), \quad (2.24)$$

$$\frac{\partial\boldsymbol{B}}{\partial k} = -2k\boldsymbol{I}. \quad (2.25)$$

Using the eigenvalues, ω, obtained by solving (2.19), saddle points are located by iterating (2.23) to zero using `Matlab`'s Newton–Raphson method `fsolve`.

2.4. *Complexity and conditioning of the numerical method*

A single iteration, which involves solving the eigenvalue problem in (2.19) as well as evaluating $\partial\omega/\partial k$ in (2.23), has a complexity of $O(N^3)$. Because such a large number of iterations are required to iterate $\partial\omega/\partial k$ to zero as the saddle point is tracked over the full extent of the $(1/\Lambda, h)$-plane of interest, the cost of each iteration must be kept as low as possible. A pseudospectral scheme is used because it requires few points, while retaining spectral accuracy. Consolidation of the equations of motion into a single fourth-order equation reduces the matrices A_{ij} and B_{ij} into smaller denser matrices as a result of the dense Chebyshev differentiation matrices, which would otherwise be larger and sparser when using primitive variables. A further factor of eight saving is made by restricting the Chebyshev basis to symmetric and antisymmetric functions so that the varicose and sinuous motions are considered separately. A symmetric basis for the streamfunction, φ, corresponds to a sinuous perturbation whereas an antisymmetric basis corresponds to a varicose perturbation. The procedure used to derive these restricted basis differentiation matrices is presented in Appendix B.

The disadvantage of using a fourth-order equation in conjunction with a pseudospectral scheme is that the condition number, a measure of a problem's amenability to digital computation, of the mth-order Chebyshev differentiation matrix scales as $O(N^{2m})$. A problem with a low condition number is said to be numerically well-conditioned, while a problem with a high condition number is said to be numerically ill-conditioned. For the fourth-order problem, the condition number scales as $O(N^8)$ whereas if primitive variables had been used, where the highest derivative is second-order, this would only be $O(N^4)$. The condition number can be significantly improved though by applying a preconditioning matrix to the generalized eigenvalue problem. The matrix

$$\Pi_{jj} = \left(1 - z_j^2\right)^2 \tag{2.26}$$

used by Huang & Sloan (1994) was shown by them to be particularly effective in conditioning fourth-order problems, reducing the condition number to only $O(N^4)$. As a result the eigenvalue problem actually solved is given by

$$\Pi\boldsymbol{A}\varphi = \omega\Pi\boldsymbol{B}\varphi. \tag{2.27}$$

Because the matrix Π_{ij} is diagonal, the cost of preconditioning the generalized eigenvalue problem prior to solving it is an insignificant $O(N^2)$ operation.

2.5. *The base flow*

This study concerns a large range of co-flow and counter-flow jets and wakes, with varying confinement, so the base flow must be sufficiently versatile to capture the full range.

Since restricted bases are used, it is necessary to solve the generalized eigenvalue problem only on the half domain $z \in [0, 1]$. As a result, the base flow needs to be defined only on this half domain and continued into the domain $z \in [-1, 0]$ by symmetry, taking care to match the profiles at $z = 0$. A similar functional form is chosen to that of the unconfined profile used by Meliga, Sipp & Chomaz (2008) with the necessary alteration to make it suitable for the confined flows studied in this

paper. It is given by

$$U(z) = 1 - \Lambda + 2\Lambda/F(z), \tag{2.28}$$

$$F(z) = 1 + \left(\frac{\beta^{((1/\eta-1)/(1/z-1))^2} - 1}{\beta - 1} \right)^\alpha, \tag{2.29}$$

where $\eta \equiv (1 - h)/2$. The squared power present in the exponent is necessary for $U''(z)$ to be continuous across $z = 0$. The base flow satisfies the following boundary conditions:

$$F(1) = \infty, \qquad U(1) = 1 - \Lambda, \tag{2.30}$$
$$F(\eta) = 2, \qquad U(\eta) = 1, \tag{2.31}$$
$$F(0) = 1, \qquad U(0) = 1 + \Lambda. \tag{2.32}$$

The range of possible flows is controlled by the three parameters, (α, β, η), which determine the location and thickness of the shear layer. The shear layer is centred about point $z = \eta$ and so is controlled by the confinement parameter h. The thickness of the shear layer can be approximated using the inverse of the velocity gradient of the profile at $z = \eta$. An asymptotic expression is given by

$$\delta \sim \frac{1}{2} \frac{\beta - 1}{\beta \ln \beta} \frac{(1 - h^2)}{\alpha}. \tag{2.33}$$

The range of possible shear-layer thicknesses is maximized when $\beta \downarrow 1$; however, for the purpose of computations the value $\beta = 1 + 10^{-6}$ is used. The thickness is then given by $\delta \sim (1/2)(1 - h^2)/\alpha$. The parameter α is then used to scale the shear-layer thickness globally; see figure 2.

The symmetries present in the base flow, $(U(z), \Lambda, h) \leftrightarrow (U(1-z), -\Lambda, -h)$, as well as in the shear-layer thickness $h \leftrightarrow -h$ are a conscious decision in anticipation of the symmetries in the absolute unstable regions calculated by Juniper (2006). Note that $h = 0$ in this study corresponds to a value of $h = 1$ in that study.

3. Spatio-temporal analysis

This section contains an outline of the procedure used to calculate transition boundaries between absolute and convective instabilities, corresponding to the linear spatio-temporal analysis. These transitions boundaries are calculated in the parameter space $(1/\Lambda, h)$ for various velocity profiles characterized by α and Reynolds number, Re.

The computations carried out use typically 50–200 collocation points. Solving the generalized eigenvalue problem in (2.19) generates a spectrum of eigenvalues, one arising for every collocation point used. Some of these eigenvalues will have converged to their true values, whereas a large proportion of the remaining eigenvalues will be spurious and require additional resolution to converge. This raises the question of which eigenvalue should be followed in order to determine the absolute–convective instability properties. It is not possible simply to consider the eigenvalue with the largest growth rate ω_i at each wavenumber value k because the primary interest is in tracking saddle points. A saddle point at wavenumber, k, for one eigenvalue need not be a saddle point at the same wavenumber for another eigenvalue. A temporal stability analysis is conducted to show which eigenvalues are important.
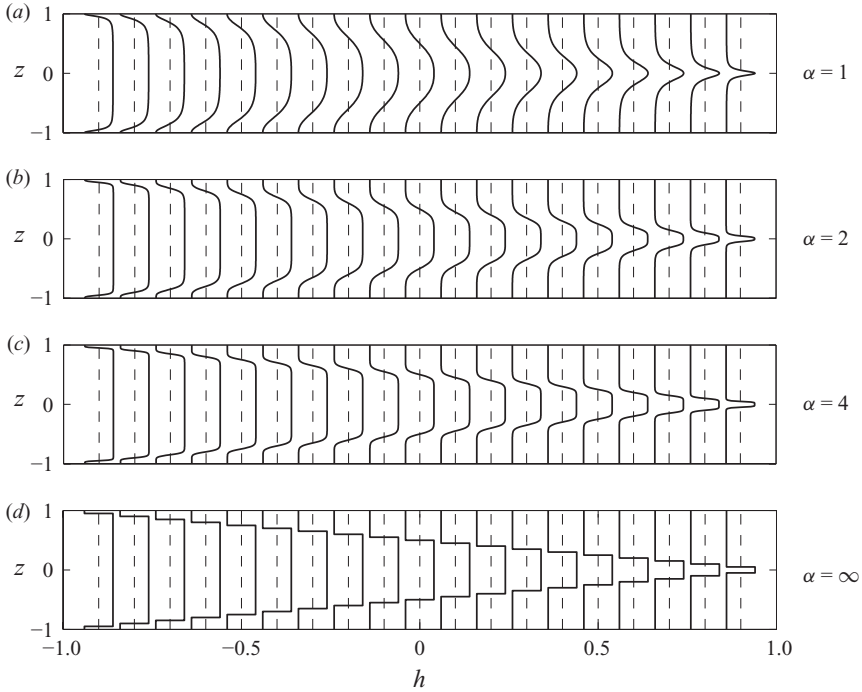
FIGURE 2. Jet profiles $U(z)$ plotted as a function of confinement, h, and the profile parameter $\alpha = 1, 2, 4$ and ∞.

3.1. *Temporal analysis*

Figure 3 shows a temporal stability analysis of sinuous perturbations for various models, plotting the growth rate ω_i against the real wavenumber k for parameters $(1/\Lambda, h) = (-1, 0)$. The first viscous eigenvalue, calculated at $Re = 1000$, shows close agreement with the inviscid smooth profile for positive growth rates. The inviscid smooth profile shares qualitative similarities with the piecewise linear profile of the same shear-layer thickness. It has the same maximum growth rate although its growth rate extends to larger values of k, which suggest that its shear layer is in fact thinner than the value calculated by the asymptotics. The inviscid plug flow profile's growth rate is unbounded since it does not possess a stabilizing mechanism but shares close agreement with the inviscid piecewise linear profile as k approaches zero. The other viscous eigenvalues, in contrast, exhibit very different behaviour from all the other profiles.

   The close agreement of the first eigenvalue of the viscous model with that of the other models motivates further investigation using asymptotics that are possible in the small wavenumber range. Drazin & Reid (1981) showed that the asymptotic dispersion relation for a momentum jet (Bickley 1937), which has a smooth unconfined $\text{sech}^2 z$ velocity profile, is the same as the unbounded plug flow jet in the long-wave limit.

3.2. *Asymptotics for long waves, $k \sim 0$*

Small wavenumbers, k, correspond to long waves. This range of wavenumbers does not hold much physical significance outside the scope of infinite-extent flows since it invalidates any parallel flow assumption. In this limit, dispersion relations for
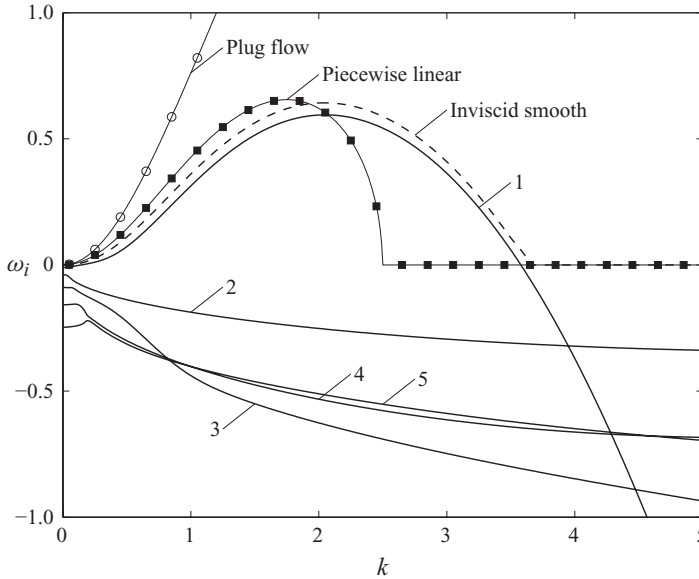
FIGURE 3. Plots of growth rate ω_i against real wavenumber k for sinuous perturbations at $(\Lambda, h) = (-1, 0)$ for (a) the inviscid plug flow profile (circles), (b) the inviscid piecewise linear profile (solid squares), (c) the inviscid smooth profile (dashed) with $\alpha = 1$ and (d) the first five eigenvalues of the viscous smooth profile (solid) for $Re = 1000$ with $\alpha = 1$, labelled 1–5.

each eigenvalue can be derived and comparisons made with the analytic dispersion relations obtained for the infinite-extent plug flow (Juniper 2006) and piecewise linear flow (Juniper 2007) in the same limit in order to determine those eigenvalues responsible for the inviscid instability.

Provided that the wavenumber satisfies $|k| \ll Re^{-1}$, an asymptotic series can be well posed in the small variable k given by

$$\varphi = \varphi_0 + k\varphi_1 + k^2\varphi_2 + \dots, \tag{3.1}$$
$$\omega = \omega_0 + k\omega_1 + k^2\omega_2 + \dots. \tag{3.2}$$

Substituting these series in the Orr–Sommerfeld equation in (2.16) and equating terms at $O(1)$ yields the leading-order differential equations

$$O(1) : \frac{i}{Re}\left(\frac{d^4}{dz^4} + i\omega_0 Re\frac{d^2}{dz^2}\right)\varphi_0 = 0, \tag{3.3}$$

subject to the boundary conditions

$$k\varphi_0 = \frac{d\varphi_0}{dz} = 0 \quad \text{at} \quad z = \pm 1. \tag{3.4}$$

Assuming that $\omega_0 \neq 0$, the varicose and sinuous solutions are respectively given by

$$\text{varicose:} \quad \varphi_0 = a_0 \sin \gamma z + b_0 z, \tag{3.5}$$
$$\text{sinuous:} \quad \varphi_0 = c_0 \cos \gamma z + d_0, \tag{3.6}$$

where $\gamma = (i\omega_0 Re)^{1/2}$. Satisfying the boundary conditions yields the following solubility criterion in both cases. The varicose solubility criterion is given by

$$\tan \gamma = \gamma, \tag{3.7}$$

which has non-zero solutions $\gamma \approx (n + (1/2))\pi$, for $n = 1, 2, \ldots$. The sinuous solubility criterion is given by

$$\sin \gamma = 0, \qquad (3.8)$$

which has exact non-zero solutions $\gamma = n\pi$, for $n = 1, 2, \ldots$. Rearranging for ω_0 gives

$$\omega_0 \sim \begin{cases} \text{varicose:} -\dfrac{\mathrm{i}(n + (1/2))^2\pi^2}{Re} \\[2mm] \text{sinuous:} \quad -\dfrac{\mathrm{i}n^2\pi^2}{Re} \end{cases} \quad n = 1, 2, \ldots. \qquad (3.9)$$

This eigenvalue spectrum describes a diverging alternating series of varicose and sinuous eigenvalues down the imaginary axis of the ω-plane. This is in excellent agreement with observed eigenvalue spectra around $k = 0$ in figure 3, which shows the sinuous case.

At the next order, $O(k)$, the governing equation is given by

$$O(k) : \frac{\mathrm{i}}{Re}\left(\frac{\mathrm{d}^4}{\mathrm{d}z^4} + \mathrm{i}\omega_0 Re \frac{\mathrm{d}^2}{\mathrm{d}z^2}\right)\varphi_1 = \left(U'' - (U - \omega_1)\frac{\mathrm{d}^2}{\mathrm{d}z^2}\right)\varphi_0. \qquad (3.10)$$

The eigenfunction φ_1 satisfies the same homogeneous equation as φ_0. This will produce secular terms if the right-hand side shares the same form as the homogeneous solution, which require a solubility criterion to remove any secular term and hence determine ω_1.

Attention is now focused on the first eigenvalue for sinuous perturbations of the viscous smooth profile, described by $(\mathrm{i}\omega_0 Re)^{1/2} = \pi$. Satisfying the boundary conditions (3.4) gives the solution to φ_0 as follows:

$$\varphi_0 = c_0(\cos \pi z + 1). \qquad (3.11)$$

The solution φ_0 will produce secular terms if the right-hand side possesses $\cos \pi z$ Fourier components. Since the differential operator on the left-hand side of (3.10) is self-adjoint, multiplying by φ_0 from the left and integrating over the domain produces the solubility criterion:

$$\int_{-1}^{1} \varphi_0\left(U'' - (U - \omega_1)\frac{\mathrm{d}^2}{\mathrm{d}z^2}\right)\varphi_0 \, \mathrm{d}z = 0. \qquad (3.12)$$

Substituting for φ_0 and rearranging for ω_1 gives

$$\omega_1 = \frac{1}{\pi^2}\int_{-1}^{1}(\cos \pi z + 1)(U''(\cos \pi z + 1) + \pi^2 U \cos \pi z)\,\mathrm{d}z. \qquad (3.13)$$

For this base flow, the integral has to be evaluated numerically, here with quadrature integration. Since the integral is real, the corresponding value of ω_1 will also be real. In order to make comparisons between the various dispersion relations in this temporal analysis using real wavenumber k, it is necessary to consider the real component of the wave frequency ω_r.

Figure 4 shows the same temporal analysis as in figure 3 plotting the real wave frequency ω_r against the real wavenumber k for parameters $(1/\Lambda, h) = (-1, 0)$. The range of k in this figure is chosen so that the previously derived asymptotics remain valid for the value of $Re = 1000$ used. The asymptotics for the first viscous eigenvalue (1) are obtained by evaluating the integral (3.13) to give a value of $\omega_1 = 2.0663$. This is in excellent agreement with the first viscous eigenvalue which itself is in close agreement with both the plug flow and piecewise linear profiles, whose asymptotic
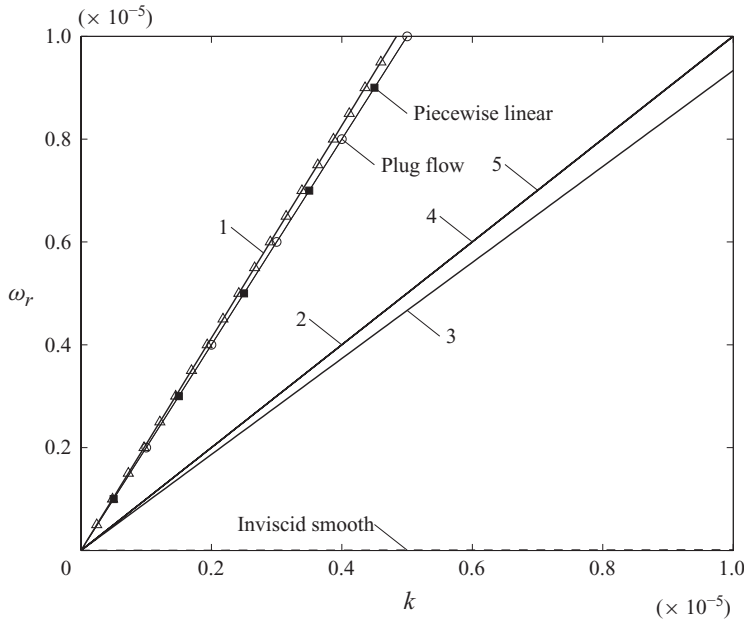
FIGURE 4. Plot of ω_r against k for sinuous perturbations at $(\Lambda, h) = (-1, 0)$ for (*a*) the inviscid plug flow profile (circles), (*b*) inviscid piecewise linear profile (solid squares), (*c*) inviscid smooth profile (dashed) with $\alpha = 1$, and (*d*) the first five eigenvalues of the viscous smooth profile (solid) for $Re = 1000$ with $\alpha = 1$, labelled 1–5. Asymptotics for the first eigenvalue of the viscous smooth profile are also plotted (triangles).

dispersion relation is given exactly by $\omega_1 = 2$. The other viscous eigenvalues (2–5) exhibit distinctly different values of ω_1 from these profiles. The inviscid smooth profile does not have a viscous term to balance it at $O(k)$ and so yields a solution $\omega_1 = 0$ as seen.

In summary, at very small wavenumbers, $k \ll O(1/Re)$, the first eigenvalue of the viscous model agrees well with those of the plug flow and piecewise linear models, as seen in figure 4. At moderate wavenumbers, $k \sim O(1)$, the first eigenvalue of the viscous model also agrees well with that of the inviscid model with smooth velocity profiles, as seen in figure 3. Figures 3 and 4 show only sinuous perturbations but the same close agreement is seen for varicose perturbations. This demonstrates that the eigenvalue that is highest at $k = 0$ is the one that needs to be considered for the analysis in this paper. As a further indication that this is the correct eigenvalue to follow, this eigenvalue is the only one to exhibit a hump in the plot of $\omega_i(k)$. This hump is the projection of a k^+ branch reaching through the k_r-axis and pinching at a saddle point with a k^- branch. This saddle point determines the behaviour in the long time limit.

3.3. *Locating and tracking saddle points*

Valid saddle points, which lie on the integration path, are formed through the pinching of a k^+ branch with a k^- branch (a pinch point). Invalid saddle points, which do not lie on the integration path, are formed through the pinching of a k^- branch with a k^- branch. The dominant saddle point is the valid saddle point with the highest value of ω_i. Pinch points can easily be identified from contours of ω_i in the complex k-plane and assessed as either dominant or sub-dominant. Figure 5 shows such contour plots
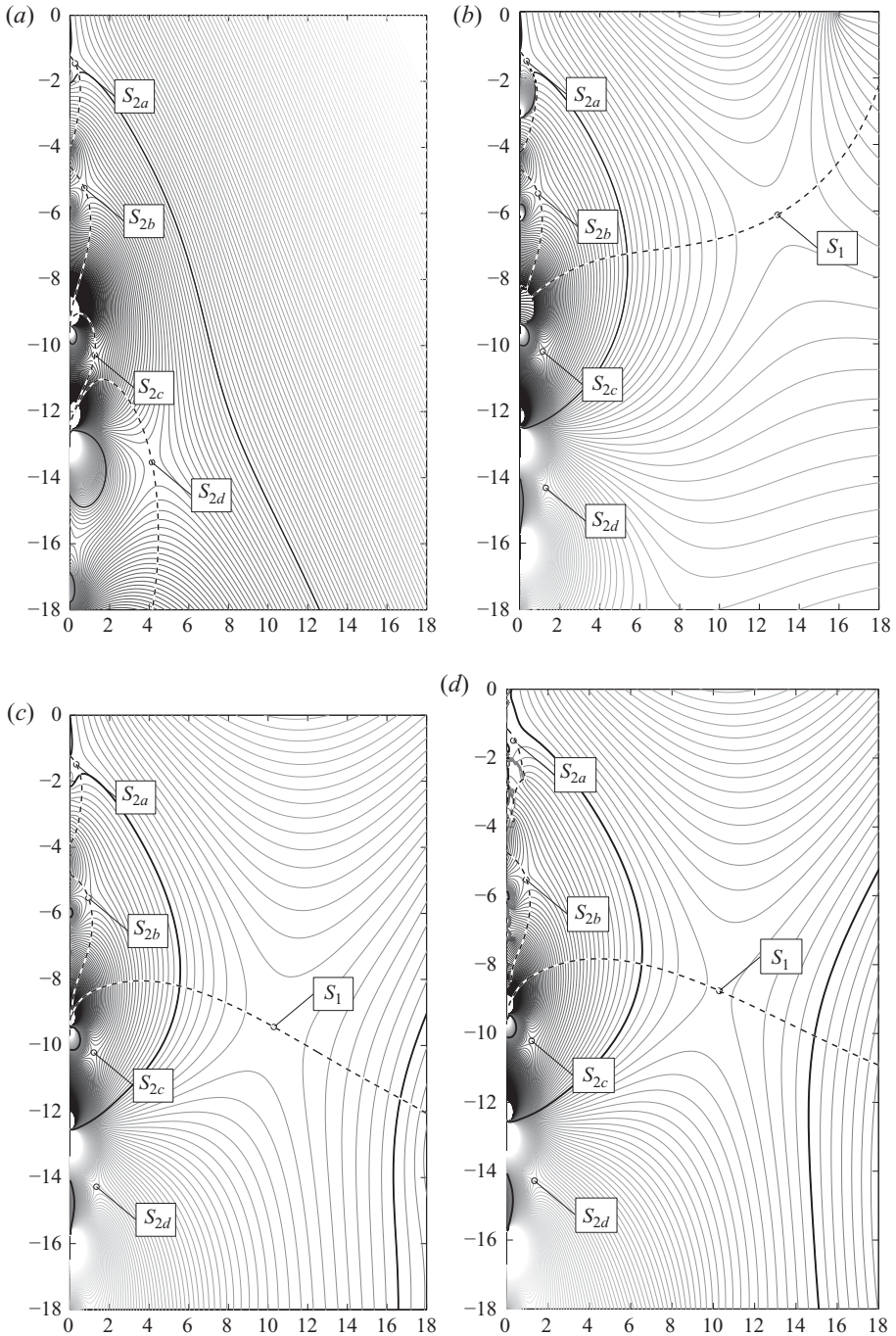
FIGURE 5. Contours of ω_i in the complex k-plane. Plots correspond to varicose perturbations of (*a*) inviscid plug flow, (*b*) inviscid finite-thickness shear layer ($\delta = 0.08$), (*c*) inviscid smooth velocity profile ($\alpha = 4$), and (*d*) viscous smooth velocity profile ($\alpha = 4$, $Re = 1000$) calculated at parameters $(1/\Lambda, h) = (0.7, -0.6)$. The solid line indicates the contour with zero growth rate, i.e. $\omega_i = 0$. Darker regions have lower growth rates and lighter regions have higher growth rates. The dashed line shows the integration contour deformed in order to take the path of steepest descent in each case.

for several different velocity profiles: (*a*) inviscid flow with a discontinuous velocity profile (plug flow), (*b*) inviscid flow with a piecewise linear velocity profile, (*c*) inviscid flow with a smooth velocity profile, and (*d*) viscous flow with a smooth velocity profile.

For the inviscid plug flow (figure 5*a*) a cascade of the saddle points, $s_{2a}, s_{2b}, \ldots$, called jet/wake column saddle points, appear near the k_i-axis. The integration path loops over an infinite number of these saddle points but, without a stabilizing mechanism, cannot return to the k_r-axis. When a finite-thickness shear layer, or any other stabilizing mechanism, is introduced (figure 5*b*) a new saddle point, s_1, appears away from the k_i-axis. Its position depends on the size of the shear-layer thickness. The integration path now loops over a finite number of the jet/wake column saddle points before passing out over this shear-layer saddle point. When a smooth velocity profile is considered (figure 5*c*) the behaviour of the integration path remains qualitatively the same, in which the path returns to the k_r-axis at negative values of ω_i. The ω_i-contours are different because of the inclusion of curvature and discrepancies in the comparative sizes of the shear layers. When viscosity is introduced into this model, the behaviour of the integration path also remains the same but the zero-contour shifts upwards, indicating that the growth rate has decreased everywhere. For instance, the s_{2a} saddle point has a positive growth rate in figure 5(*c*), which is inviscid, but a negative growth rate in figure 5(*d*), which is viscous.

The analytic dispersion relations for inviscid plug flows and finite-thickness shear-layer profiles produce two solutions for ω. The correct solution can easily be selected at every point in the complex k-plane. For the smooth velocity profiles, both inviscid and viscous solutions are obtained numerically and there are as many solutions for ω as there are collocation points. This makes it difficult to select the correct solution at every point in the complex k-plane.

For the inviscid problem, solutions are complex conjugates pairs and often the solution with the highest ω_i provides the correct solution over a sufficiently large region of the k-plane. For the viscous problem, the structure of the solutions is different and around $k = 0$ the solutions are very close together ($O(Re^{-1})$ apart), making it difficult to follow any particular solution. At high Re and away from $k = 0$, the inviscid solution provides a suitable starting point for the location of the desired viscous solution. At low Re, solutions are sufficiently far apart that the solution with the highest ω_i at $k = 0$ can be tracked to every point in the k-plane by taking steps of size $O(Re^{-1})$.

Using these contour plots, the location of a saddle point can be estimated and then accurately determined by solving (2.27) whilst simultaneously searching for a zero of (2.23). The parameter Λ is then varied, whilst keeping track of the saddle, until the growth rate becomes zero, i.e. $\omega_i^s = 0$. Rather than vary h, Λ is varied because the absolute–convective transition boundary is guaranteed to be intercepted.

The absolute–convective transition boundary in the (Λ, h)-space is the curve along which the growth rate of the saddle remains zero and can be represented parametrically by

$$\omega_i^s(\Lambda(\tau), h(\tau)) = 0, \qquad (3.14)$$

where τ is the parametric variable. Note that ω_i^s no longer depends on k since it is constrained to be a saddle point given by $\partial \omega^s / \partial k = 0$ for all t. Using this parametric form, saddle points can be followed whilst keeping their growth rate zero in order to produce absolute–convective transition boundaries. Further details of this method are given in Appendix C.

4. The effect of shear-layer thickness

In this section, the effect of shear-layer thickness on the absolute instability is determined in the $(1/\Lambda, h)$-space. Inviscid flow is considered so that comparisons can be made with the inviscid plug flow and piecewise linear calculations in Juniper (2006) and Juniper (2007). When $Re = \infty$, the Orr–Sommerfeld equation (2.16) becomes the Rayleigh equation

$$(U - c)\left(\frac{d^2}{dz^2} - k^2\right)\varphi - \frac{d^2 U}{dz^2}\varphi = 0, \tag{4.1}$$

subject only to the no-flux boundary conditions

$$k\varphi = 0 \quad \text{at} \quad z = \pm 1. \tag{4.2}$$

Figure 6 shows regions of absolute instability in the $(1/\Lambda, h)$-space for varicose and sinuous perturbations. Plots are calculated for four different shear-layer thicknesses, characterized by the profile parameter α.

The case with $\alpha \to \infty$ is shown in figure 6(a). This corresponds to a jet/wake flow with infinitely thin piecewise linear shear layers, as studied by Juniper (2007). The absolute–convective transition boundaries at $1/\Lambda = \pm 1$ arise from contributions from the infinitely thin shear-layer mode. The other lines, at which ω_i^s is also equal to zero, arise from contributions from the jet/wake column modes. For varicose perturbations, the absolutely unstable regions exhibit the symmetry $(\Lambda, h) \leftrightarrow (-\Lambda, -h)$, and the shear-layer mode dominates the instability causing all counter-flow to be absolutely unstable. For sinuous perturbations, the absolutely unstable regions exhibit the symmetry $(\Lambda, h) \leftrightarrow (\Lambda, -h)$ and, although the shear-layer mode largely dominates in the same way as for varicose perturbations, the principal jet/wake column mode dominates for wakes at confinement around $h \approx 0$ and gives rise to a large region of absolute instability that extends far into the co-flow domain.

For $\alpha = 1$, corresponding to the velocity profile with the thickest shear layer, the shear-layer saddle lies close to the origin. It and the principal jet/wake column mode saddle are the only saddles that lie on the integration contour. For varicose perturbations, the shear-layer saddle is always the dominant saddle, although the sub-dominant jet/wake column mode saddle influences the region of absolute instability that it produces. This influence can be seen in weakly confined wakes and strongly confined jets, for which the absolutely unstable region follows the line where the principal jet/wake column mode at $\alpha \to \infty$ has zero growth rate (the nearly straight diagonal lines in figure 6a). For sinuous perturbations, the principal jet/wake column mode contributes directly to the absolutely unstable region, producing a hump at $h \sim 0$ that extends into the co-flow wake domain, similar to that found in the $\alpha \to \infty$ case. At strong confinement, the absolutely unstable regions due to the shear-layer mode are similar to those of the varicose perturbations because, at strong confinement, the shear layer is most strongly influenced by its image in the wall. At weak confinement, the sinuous behaviour is very different from the varicose behaviour and, for wakes, the absolutely unstable region extends into the co-flow region, suggesting that a finite thickness shear layer is more unstable than an infinitely thin shear layer. This observation agrees with results in figure 6 of Lesshaft & Huerre (2007).

As the shear-layer thickness decreases (increasing α), the shear-layer saddle moves away from the k_i-axis. This allows the integration path to pass over additional jet/wake column mode saddles before passing out over the shear-layer saddle. The thinning of the shear layers significantly enhances absolute instability, causing the absolutely unstable regions to extend to lower values of shear. For varicose perturbations, this
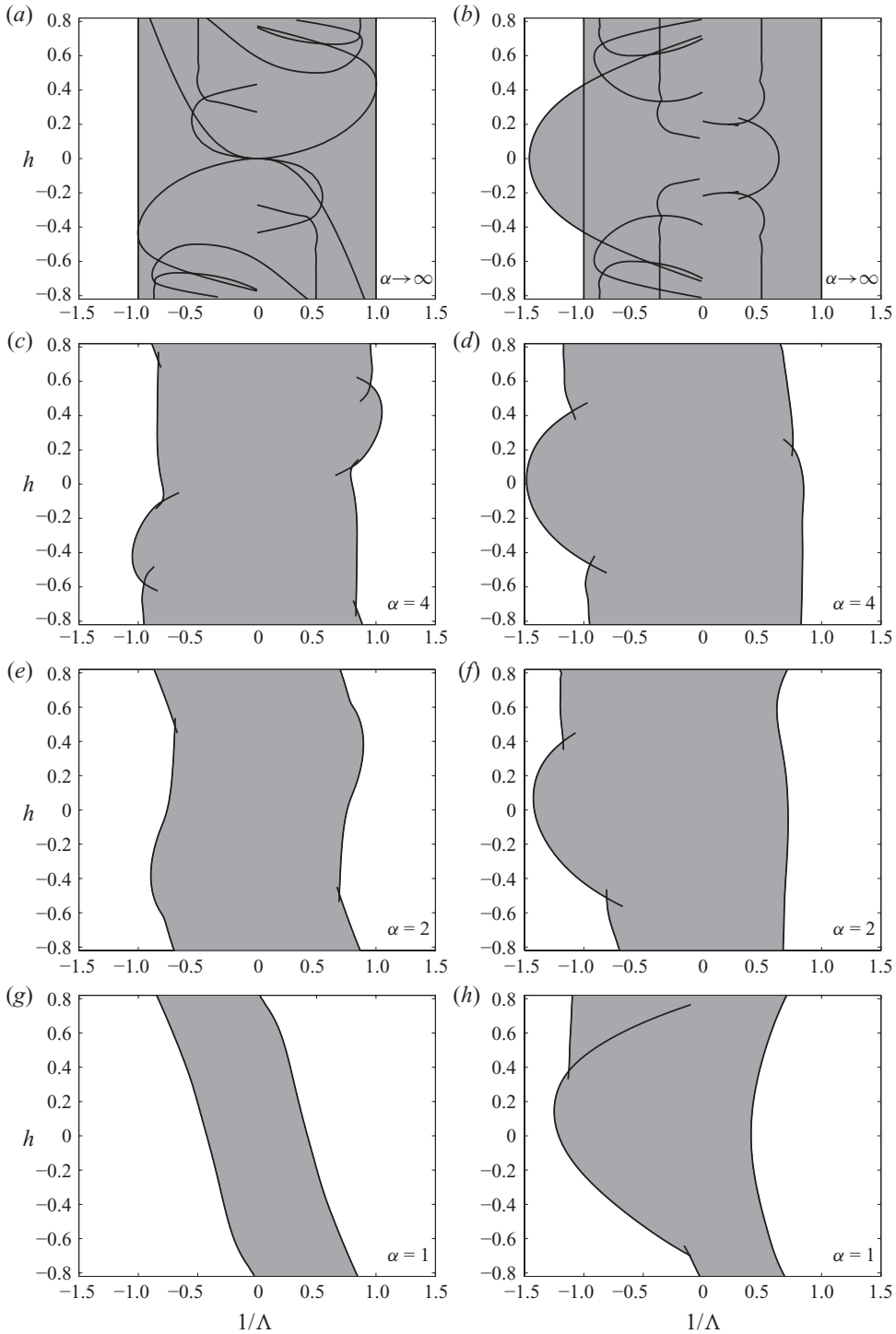
FIGURE 6. Regions of absolute instability (grey) plotted in the $(1/\Lambda, h)$-space for inviscid flow subject to varicose perturbations (left) and sinuous perturbations (right). Plots correspond to velocity profiles with different shear-layer thicknesses described by the profile parameter $\alpha = \infty, 4, 2, 1$.

occurs for strongly confined wakes as well as weakly confined jets because of the varicose symmetry $(\Lambda, h) \leftrightarrow (-\Lambda, -h)$.

When $\alpha = 4$, the absolutely unstable regions for both varicose and sinuous perturbations bear a close resemblance to their counterparts when $\alpha \to \infty$. The absolute–convective transition boundaries from the shear-layer mode approach the values $1/\Lambda = \pm 1$, which they take in the limit $\alpha \to \infty$. For weakly confined sinuous wakes, the absolutely unstable regions continue to extend significantly into the co-flow domain. In addition, prominent features arising from the jet/wake modes can be identified. For varicose perturbations, the asymmetric humps (around $h \approx -0.4$ for wakes and $h \approx 0.4$ for jets) extend into the co-flow domain, demonstrating that a finite thickness shear layer promotes instability. For sinuous perturbations, the large wake-side hump has the approximate symmetry $(\Lambda, h) \leftrightarrow (\Lambda, -h)$ and, like the varicose case, extends marginally further outwards.

5. The effect of viscosity

In this section, the effect of viscosity on absolute instability is determined. Regions of absolute instability are calculated in the $(1/\Lambda, h)$-space for different values of the Reynolds number between 10 and 1000. The $\alpha = 4$ velocity profile is considered throughout this section because, with this thinner shear layer, both jet/wake column modes and the shear-layer modes can be identified.

Figures 7 and 8 show regions of absolute instability in the $(1/\Lambda, h)$-space of this viscous flow for varicose and sinuous perturbations respectively. Plots are calculated at six different values of the Reynolds numbers, $Re = \infty$, 10^3, $10^{2.5}$, 10^2, $10^{1.5}$ and 10^1.

The $Re = \infty$ plots correspond to the inviscid calculations in the previous section. The asymptotics in §3.2 showed that, when viscosity is introduced, the growth rate, ω_i, becomes negative near the origin. These values differ from the inviscid value of $\omega_i = 0$ by $O(Re^{-1})$. The temporal analysis in figure 3 shows that, away from the origin, the behaviour follows that of the inviscid curve, although at lower values of ω_i. Therefore, the inviscid curve provides an upper bound on the viscous behaviour away from the origin. The overall effect throughout the complex k-space seen in figure 5(d) (viscous) when compared with figure 5(c) (inviscid) is that contours of ω_i are lowered everywhere.

When viscosity is introduced, a new saddle appears close to the origin, for sinuous perturbations. This saddle produces a large region of absolute instability on the jet side, which is shaded light grey in figure 8. The relevance and behaviour of this saddle is discussed in §5.1.

With weak viscosity, corresponding to $Re = 1000$, the regions of absolute instability (shaded dark grey) for both varicose and sinuous perturbations are only slightly different from those of the inviscid flow. At higher Reynolds numbers this difference is even less, as can be seen in figure 9, which shows the growth rate of a saddle as a function of Reynolds numbers for different shear-layer thicknesses. Above $Re = 1000$, the behaviour of the growth rate is approximated well by its inviscid value, whilst below $Re = 100$ the behaviour is dominated by viscous effects and the growth rate decreases rapidly. In between these two values the behaviour is a combination of the two.

As the Reynolds number decreases from 1000 to 10, the regions of absolute instability contract towards $1/\Lambda = 0$, which corresponds to strong counter-flow. Transition boundaries are most strongly affected at both strong and weak confinement ($h \sim \pm 0.82$). This is because the shear-layer thickness is one-third of its value at
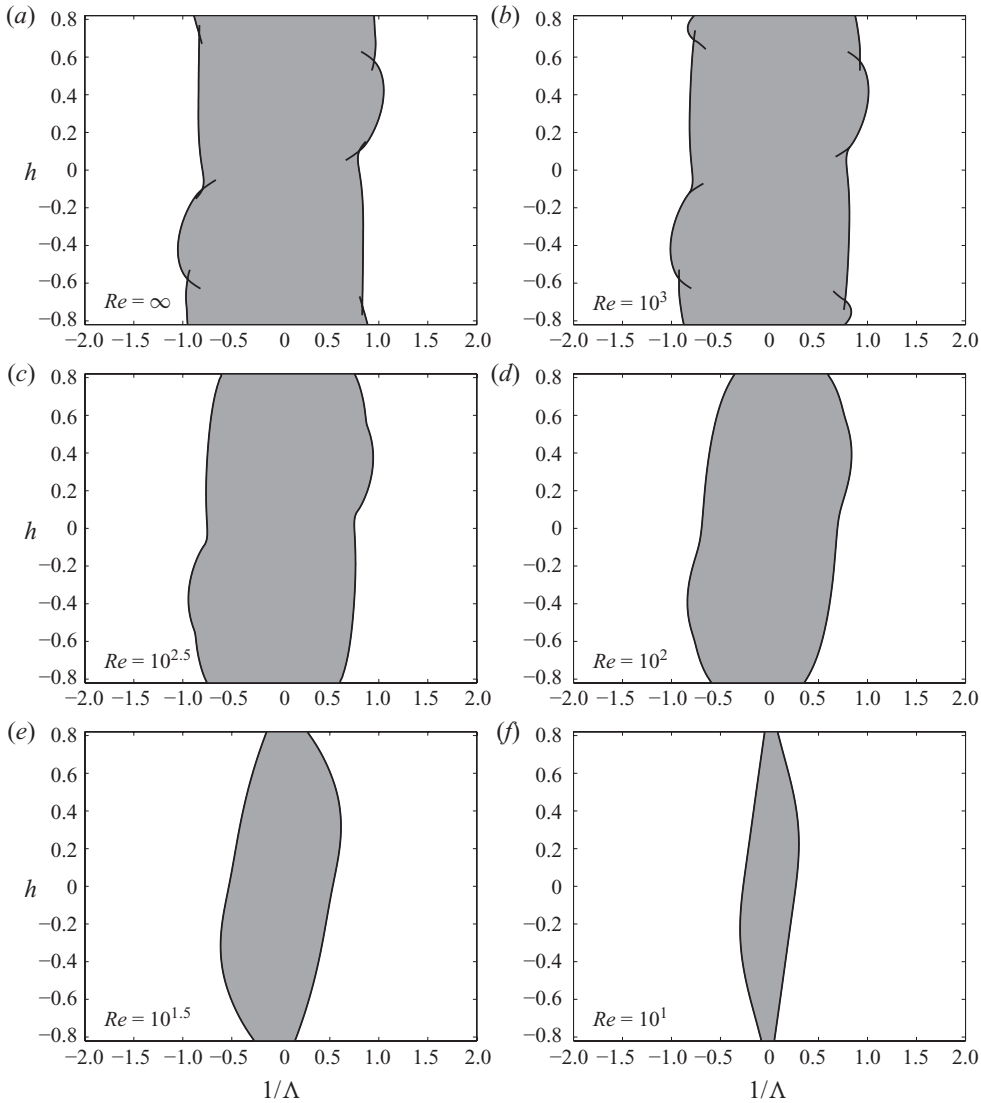
FIGURE 7. Regions of absolute instability (grey) in the $(1/\Lambda, h)$-space for viscous flow subject to varicose perturbations. Plots are calculated for the profile parameter $\alpha = 4$ over a range of different Reynolds numbers, $Re = \infty$, 10^3, $10^{2.5}$, 10^2, $10^{1.5}$ and 10^1.

normal confinement ($h \sim 0$), which causes the shear-layer saddle to move to larger values of k, on which viscosity has a stronger stabilizing effect. At each Reynolds number, the regions of absolute instability for varicose perturbations continue to obey the symmetry $(1/\Lambda, h) \leftrightarrow (-1/\Lambda, -h)$. Similarly, regions of absolute instability for sinuous perturbations at strong confinement continue to match those in the varicose case.

Optimal confinement is defined as the confinement at which absolute instability occurs with the lowest amount of shear (largest $|1/\Lambda|$). For varicose perturbations, this occurs around $h \approx 0.4$ for jets and $h \approx -0.4$ for wakes and continue to remain around these values as the Reynolds number decreases. For sinuous perturbations,
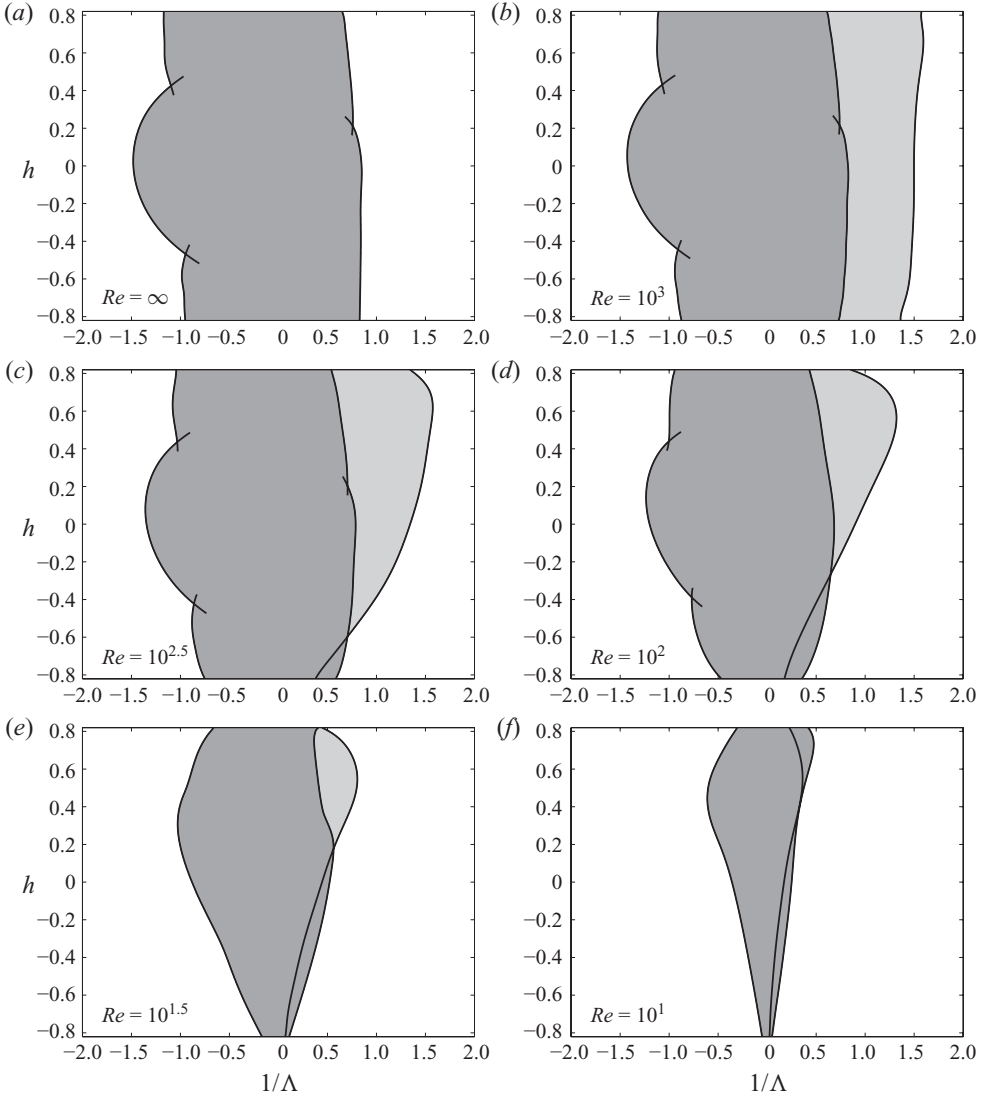
FIGURE 8. Same as figure 8 but for sinuous perturbations. Regions of absolute instability shaded in light grey are produced by the viscous saddle described in § 5.1, which has a very small growth rate.

this occurs around $h = 0$ but shifts to weaker values of confinements as the Reynolds number is decreased.

5.1. *Long-wavelength viscous saddle*

For sinuous jets, a new saddle point appears. This can be seen in figure 10, which shows plots of growth rate, ω_i, in the k-plane at five different Reynolds numbers: $10^1, 10^{1.5}, 10^2, 10^{2.5}, 10^3$. The plots indicate that the saddle point is a legitimate k^+/k^- pinch point and that it goes absolutely unstable between $Re = 10^{1.5}$ and 10^2.

The region of absolute instability generated by this saddle point is shown as a function of Reynolds number in figure 10(*f*). As the Reynolds number increases, the
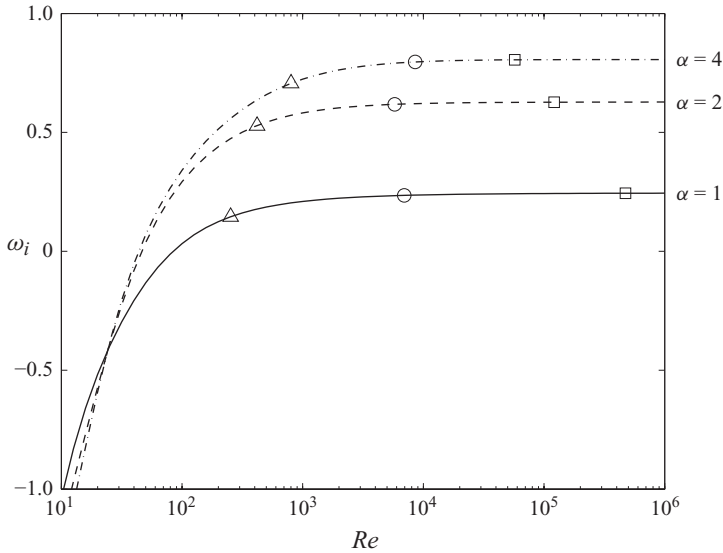
FIGURE 9. Plots of ω_i of the principal jet/wake column mode saddle at $(1/\Lambda, h) = (-1, 0)$ for sinuous perturbations as the Reynolds number is varied between 10 and 10^6. Growth rates are plotted for three different velocity profiles, $\alpha = 1$ (solid), 2 (dashed) and 4 (dot dashed). The markers indicate where the value of ω_i is within a tolerance of 0.1 ($\triangle$), 0.01 ($\bigcirc$) and 0.001 ($\square$) of its value for $Re = \infty$.

absolutely unstable region includes co-flow jets and becomes larger than the region generated by the shear layer and flow mode saddles alone.

Figure 11 shows the frequency, growth rate and wavenumber of this saddle as the Reynolds number varies. The growth rate is a maximum around $Re = 10^3$. As the Reynolds number increases further, the growth steadily decreases and the saddle point moves closer to $k = 0$. At high Reynolds numbers, both k_r and k_i scale with $Re^{-1/2}$ and ω_i scales with Re^{-1}. These power laws indicate that, in addition to having a very long wavelength, the viscous mode has very small growth rates.

This saddle point does not appear in the inviscid calculations and strongly depends on the Reynolds number, so we call this the viscous saddle point, s_0. A global analysis might reveal a corresponding viscous global mode but, with such a weak growth rate, it could prove to be as difficult to observe as the most unstable Orr–Sommerfeld mode in a planar Poiseuille flow just above a Reynolds number of 5772. It is curious but seems unlikely to be influential in a global analysis.

5.2. *Effect of boundary layers*

As well as changing the stability of a flow through the mechanisms described by Juniper (2007), confinement alters the base flow by introducing boundary layers. In the global analysis of Tammisola (2009), confined wake flows with perfect slip are considered alongside confined wake flows with no slip. Tammisola (2009) finds that the former flows, which have no boundary layers, are destabilized by confinement while the latter flows, which have developing boundary layers, are stabilized by confinement. The former result agrees with those in this paper, in which boundary layers are avoided by moving the confining walls with the fluid. The latter result raises the question of whether an interaction between the shear layers and the boundary layers has caused the flow to become more stable or whether this stabilizing effect
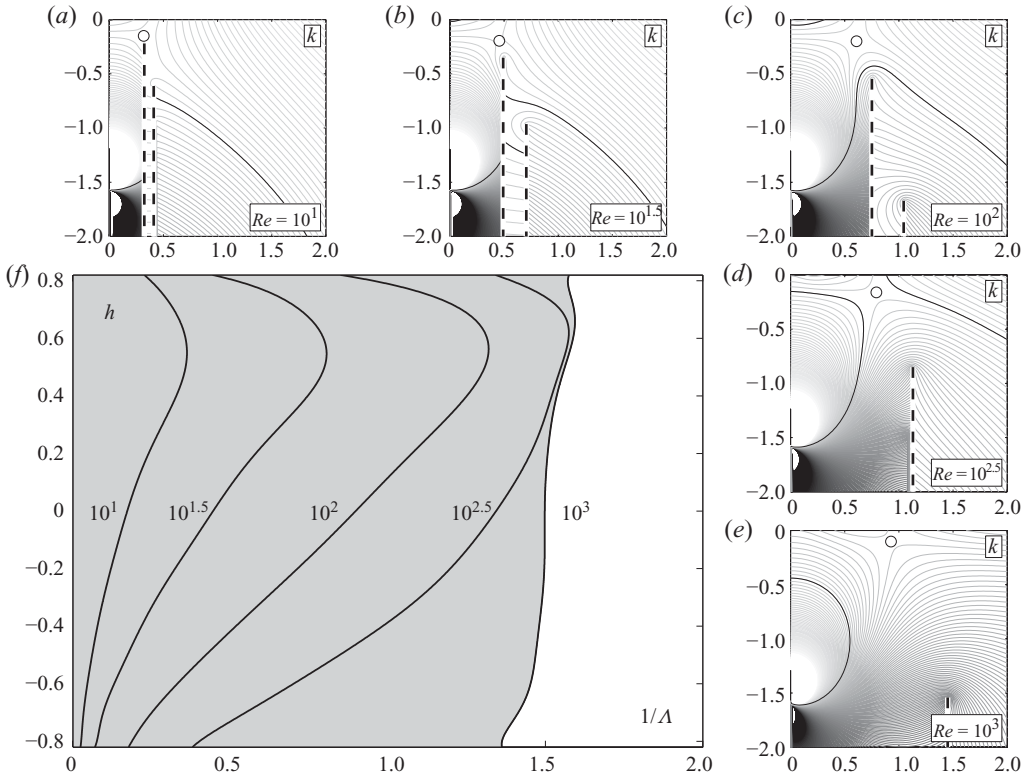
FIGURE 10. Small plots $(a–e)$ show contours of the growth rate ω_i in the complex k-space calculated for $(1/\Lambda, h, \alpha) = (0.5, 0, 4)$ at five different Reynolds numbers, $Re = 10^1, 10^{1.5}, 10^2, 10^{2.5}, 10^3$. The position of the viscous saddle point is indicated by the black circle and can be seen to remain a valid pinch point across all Reynolds numbers. The $\omega_i = 0$ contour is shown as a solid line. Branch cuts are shown as dashed lines. (f) The large plot shows the regions of absolute instability as a function of confinement and shear corresponding to the viscous saddle point at the different Reynolds numbers labelled on each contour.

arises simply because the boundary layers cause the flow to relax towards Poiseuille flow.

In order to investigate this, four of the no-slip confined cases in Tammisola (2009) are analysed here. First, the local stability of the entire profile is calculated, containing both the shear layers and the boundary layers. Then the boundary layers are artificially removed and the local stability is recalculated. Both the temporal and the absolute growth rates are calculated for each profile as shown in figure 12.

When the boundary layers are far from the shear layers, they have a negligible effect on both growth rates. This can be seen over the approximate ranges $0 < x < 6$ for $h = 0.6$ and 0.4 and $0 < x < 0.5$ for $h = 0.2$ and 0.0. The upstream region, $0 < x < 0.5$, clearly becomes more unstable as the flow is confined, in accordance with the results of this paper. When the boundary layers start to impinge on the shear layers, however, they reduce both growth rates. This can be seen clearly particularly over the range $1 < x < 3$ for $h = 0.0$. This occurs before the boundary layers have reached Poiseuille flow, so must be due to an interaction between the shear layers and the boundary layers.
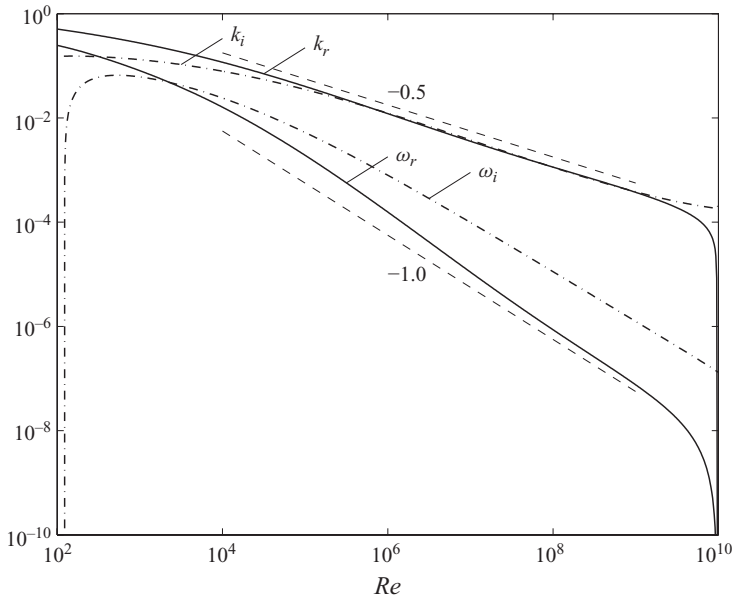
FIGURE 11. The properties ω_r, k_r (solid) and ω_i, k_i (dot-dashed) of the long-wavelength saddle are tracked as the Reynolds number is varied between 10^2 and 10^{10} for the parameters $(1/\Lambda, h) = (1, 0)$.

6. Conclusions

In this paper, a model base flow has been used to examine the effect of shear-layer thickness and viscosity on the absolute instability of a wide range of confined planar jets and wakes. The primary aim of this study is to catalogue the effect of confinement on viscous flows. The secondary aim is to examine the effect of the Reynolds number on confined flows in order to determine the valid range of inviscid models such as those of Juniper (2006). The tertiary aim is to examine the effect of the shear-layer thickness in order to determine whether a piecewise linear shear layer can capture the important points of the instability behaviour or whether the exact profile is required. A spatio-temporal analysis was conducted to determine regions of absolute instability in the $(1/\Lambda, h)$-space of interest. Results were obtained over a wide range of confinements $-0.82 < h < 0.82$ corresponding to $0.1 < h_2/h_1 < 10$.

First, the effect of shear-layer thickness was examined, taking the fluid to be inviscid. For the most part, thicker shear layers stabilize the flow. A finite-thickness shear layer can, however, enhance the absolute instability relative to the infinitely thin shear layer for both varicose and sinuous perturbations. With a thin shear-layer thickness ($\alpha = 4$) the absolutely unstable regions closely match those calculated using a plug flow and piecewise linear profile. This can be seen by comparing figures 6(a) and 6(c) for varicose perturbations and 6(b) and 6(d) for sinuous perturbations. This suggests that the simple models used in previous studies by Juniper (2006, 2007) provide good approximations for instability properties when the shear-layer thickness is thin, which achieves the tertiary aim of the study. The region with thin shear layers would correspond to the region immediately downstream of where the two streams are introduced. The local instability properties in this region have a strong influence on the global instability.
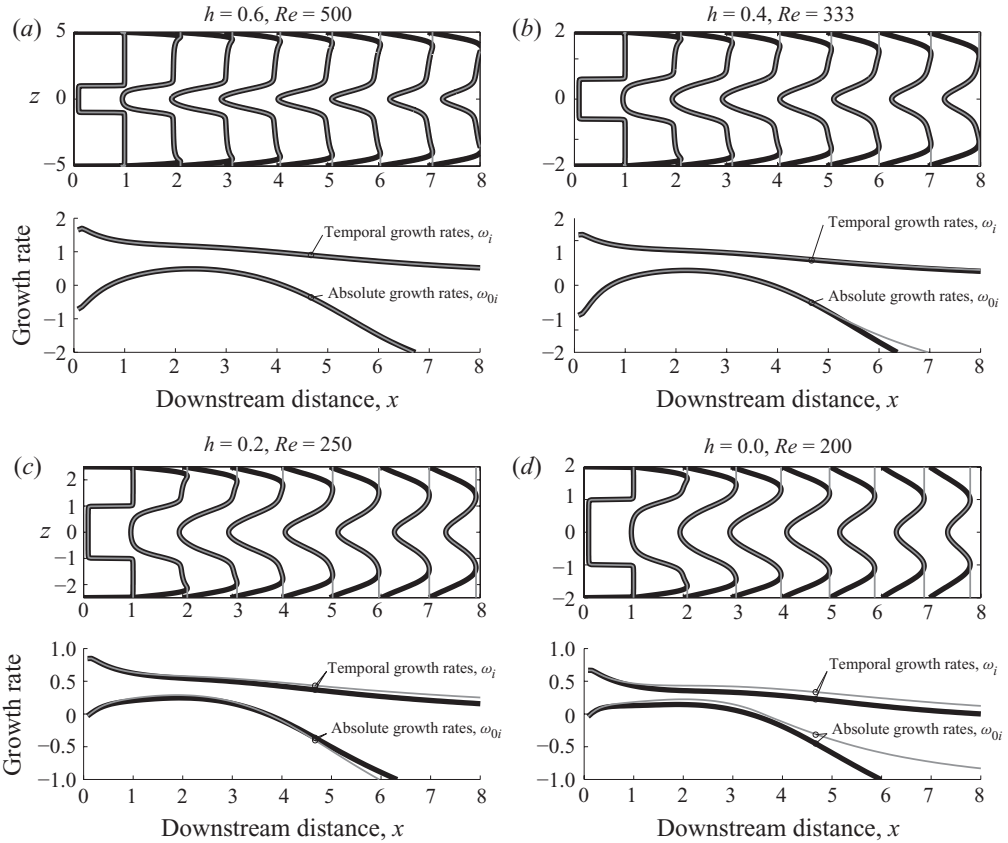
FIGURE 12. (*a*–*d*) The local stability of base flows with and without boundary layers for $h = 0.6, 0.4, 0.2$ and 0.0. The velocity profiles (top) and local growth rates (bottom) are shown as functions of downstream distance for the cases with boundary layers (black) and without boundary layers (grey). The boundary layers are removed by replacing the velocity in the boundary layer with the maximum velocity. The base flows are calculated at $Re = 100$ based on the half-width of the wake and the maximum inlet velocity of the outer flow. This corresponds to $Re = 500, 333, 250$ and 200 based on the width of the channel.

Second, the effect of viscosity was examined on the thinnest shear-layer profile ($\alpha = 4$). In the first step, the absolutely unstable region in $(1/\Lambda, h)$-space was determined for $10 \leqslant Re \leqslant 10^3$ and compared with that determined for the inviscid case. It was observed that, as the Reynolds number decreases, the regions of absolute instability shrink towards $1/\Lambda = 0$, which corresponds to a very strong counter-flow. The regions retain, however, their general dependence on confinement, h. In the second step, the growth rate of the principal jet/wake column mode was determined at $(1/\Lambda, h) = (-1, 0)$ for three shear-layer thicknesses with $10 \leqslant Re \leqslant 10^6$. It was observed that the Reynolds number has little effect above $Re = 10^3$, which achieves the secondary aim of the study. For the sinuous instability, a viscous mode was discovered with a very long wavelength and a very small growth rate. Although valid within the constraints of the model, particularly the constraint of no streamwise evolution, it seems unlikely that this mode would be influential in an experiment or a global stability analysis.

The primary aim of this study is to examine the effect of confinement on viscous flows. At each Reynolds number, an optimal value of confinement was found at which absolute instability could occur for the least amount of shear (largest $|1/\Lambda|$). For varicose perturbations, the optimal confinement was located around $h \approx 0.4$ ($h_2/h_1 \approx 7/3$) for jets and $h \approx -0.4$ ($h_2/h_1 \approx -7/3$) for wakes, over the majority of the range of Reynolds numbers considered. For sinuous perturbations, the optimal confinement was located at $h \approx 0$ ($h_2/h_1 \approx 1$) for both jets and wakes at large Reynolds numbers ($Re \geqslant 1000$) but was found to prefer weaker confinement as the Reynolds number was decreased. It is natural to examine the effect of confinement at a given Reynolds number. When this Reynolds number is defined by the width of the channel, this study shows that confinement has the same destabilizing effect on viscous flows that it has on inviscid flows, until the boundary layers start to impinge on the shear layers. This theoretical result is consistent with the experimental findings of Shair *et al.* (1963), Chen *et al.* (1995) and Davis *et al.* (1983).

This paper is one of a series investigating the most influential factors affecting the stability of jet/wake flows. The main emphasis of this paper is the effect of viscosity and confinement. At $Re = 1000$, regions of absolute instability in $(1/\Lambda, h)$-space are found to coincide closely with those for inviscid flow. It can also be inferred from the results in this paper that this agreement will improve with increasing Re. This result has important implications for the study of confined jet/wake flows at high Reynolds numbers, regardless of whether Re is based on the channel width or the jet/wake width. This is because the assumption of vanishing vorticity makes the stability analysis much simpler and cheaper. Flows in this category include the flow within combustion chambers in rockets and aircraft, particularly the flow just downstream of the fuel injectors, where the Reynolds number is typically 10^5.

Appendix A. Collocation method and Chebyshev basis functions

Chapters 4–6 of Boyd (2000) provide an extensive description of spectral methods used in this paper. A Chebyshev–Gauss–Lobatto grid constructed with $2N$ points is given by

$$z_j = \cos\left(\frac{\pi(j-1)}{2N-1}\right), \qquad j = 1, 2, \ldots, 2N. \tag{A 1}$$

A cardinal basis, using Chebyshev polynomials, is defined on this grid by the functions

$$C_j(z) = \frac{(1-z^2)^2}{\left(1-z_j^2\right)^2} \frac{T'_{N-1}(z)}{T''_{N-1}(z_j)(z-z_j)}, \qquad j = 1, 2, \ldots, 2N, \tag{A 2}$$

such that $C_j(z_i) = \delta_{ij}$. Chebyshev polynomials, $T_N(z)$, are solutions of the equation

$$(1-z^2)T''_N - zT'_N + N^2 T_N = 0. \tag{A 3}$$

The leading quartic term in (A 2) ensures that the Dirichlet ($C_j(\pm 1) = 0$) and Von Neumann ($C'_j(\pm 1) = 0$) boundary conditions are satisfied at both walls by every cardinal function and so also by any combination of them. The nth differentiation matrix is constructed as follows:

$$D_{ij}^{(n)} = C_j^{(n)}(z_i), \qquad i, j = 1, 2, \ldots, 2N. \tag{A 4}$$

They are produced using the program `cheb4c.m`, found in a MATLAB differentiation matrix suite developed by Weideman & Reddy (2000).

Appendix B. Restriction to a symmetric or antisymmetric basis

Exploiting parity is described in chapter 8 of Boyd (2000). The full cardinal basis, $C_j(z)$, is defined on the domain, $z \in [-1, 1]$, corresponding to $j = 1, 2, \ldots, 2N$. Restricting the basis to only symmetric or antisymmetric functions restricts consideration to the half-domain, $z \in [0, 1]$, corresponding to $j = 1, 2, \ldots, N$. Symmetric basis functions, $S_j(x)$, and antisymmetric basis functions, $A_j(x)$, are constructed from the original cardinal basis, $C_j(z)$, as follows:

$$S_j(z) = C_j(z) + C_j(-z), \qquad j = 1, 2, \ldots, N, \tag{B 1}$$
$$A_j(z) = C_j(z) - C_j(-z), \qquad j = 1, 2, \ldots, N. \tag{B 2}$$

The nth differentiation matrix for the restricted bases, $D_S^{(n)}$ (symmetric) and $D_A^{(n)}$ (antisymmetric), is obtained by differentiating each basis function and evaluating it at each point in the half-domain, z_i, for $i = 1, 2, \ldots, N$:

$$S_j^{(n)}(z_i) = C_j^{(n)}(z_i) + (-1)^n C_j^{(n)}(-z_i), \qquad i, j = 1, 2, \ldots, N, \tag{B 3}$$
$$A_j^{(n)}(z_i) = C_j^{(n)}(z_i) - (-1)^n C_j^{(n)}(-z_i), \qquad i, j = 1, 2, \ldots, N. \tag{B 4}$$

Using the symmetry of the Chebyshev–Gauss–Lobatto grid, $C_j^{(n)}(-z_i) = C_j^{(n)}(z_{N-i})$ for all n gives

$$\left(D_S^{(n)}\right)_{ij} = D_{ij}^{(n)} + (-1)^n D_{(N-i)j}^{(n)}, \qquad i, j = 1, 2, \ldots, N, \tag{B 5}$$
$$\left(D_A^{(n)}\right)_{ij} = D_{ij}^{(n)} - (-1)^n D_{(N-i)j}^{(n)}, \qquad i, j = 1, 2, \ldots, N. \tag{B 6}$$

Appendix C. Parametric saddle-point equations

In order to remain on the transition boundary, the saddle point must satisfy $d\omega_i^s / d\tau = 0$ given by

$$\frac{d\Lambda}{d\tau} \left(\frac{\partial \omega_i^s}{\partial \Lambda}\right)_h + \frac{dh}{d\tau} \left(\frac{\partial \omega_i^s}{\partial h}\right)_\Lambda = 0. \tag{C 1}$$

A further condition is required to obtain both branches of the solution, i.e. those increasing and decreasing with h, given by $dh/d\tau = \pm 1$, respectively. This system of equations can be expressed in matrix form as

$$\begin{pmatrix} \left(\dfrac{\partial \omega_i^s}{\partial \Lambda}\right)_h & \left(\dfrac{\partial \omega_i^s}{\partial h}\right)_\Lambda \\ 0 & 1 \end{pmatrix} \begin{pmatrix} \dfrac{d\Lambda}{d\tau} \\ \dfrac{dh}{d\tau} \end{pmatrix} = \begin{pmatrix} 0 \\ \pm 1 \end{pmatrix}, \tag{C 2}$$

which can also be trivially inverted to give

$$\begin{pmatrix} \dfrac{d\Lambda}{d\tau} \\ \dfrac{dh}{d\tau} \end{pmatrix} = \begin{pmatrix} \mp \left(\dfrac{\partial \omega_i^s}{\partial h}\right)_\Lambda \left(\dfrac{\partial \omega_i^s}{\partial \Lambda}\right)_h^{-1} \\ \pm 1 \end{pmatrix}. \tag{C 3}$$

Along with a suitably accurate initial condition, $(\Lambda(\tau_0), h(\tau_0)) = (\Lambda_0, h_0)$, this is now in an appropriate form for solving using an ODE solver. The partial derivatives on the

right-hand side cannot be obtained analytically and so have to be approximated by finite difference schemes. In both cases, a simple Euler difference scheme is adopted as follows:

$$\frac{\mathrm{d}\Lambda}{\mathrm{d}\tau} = \mp \left(\frac{\partial \omega_i^s}{\partial h}\right)_\Lambda \left(\frac{\partial \omega_i^s}{\partial \Lambda}\right)_h^{-1} = -\frac{\delta\Lambda}{\delta h}\left(\frac{\omega_i^s(\Lambda, h \pm \delta h) - \omega_i^s(\Lambda, h)}{\omega_i^s(\Lambda + \delta\Lambda, h) - \omega_i^s(\Lambda, h)}\right) + O(\delta\Lambda, \delta h),$$

(C 4)

because the quantities $\delta\Lambda$ and δh can be taken to be arbitrarily small so as to achieve the required accuracy.

REFERENCES

BEARMAN, P. W. & ZDRAVKOVICH, M. 1978 Flow around a circular cylinder near a plane boundary. *J. Fluid Mech.* **89**, 33–47.

BICKLEY, W. G. 1937 The plane jet. *Phil. Mag.* **26** (6), 727–731.

BOYD, J. P. 2000 *Chebyshev and Fourier Spectral Methods*, 2nd edn. Springer.

CAMARRI, S. & GIANNETTI, F. 2007 On the inversion of the von Kármán street in the wake of a confined square cylinder. *J. Fluid Mech.* **574**, 169–178.

CHEN, J.-H., PRITCHARD, W. G. & TAVENER, S. J. 1995 Bifurcation for flow past a cylinder between parallel planes. *J. Fluid Mech.* **284**, 23–41.

CHOMAZ, J.-M., HUERRE, P. & REDEKOPP, L. 1988 Bifurcations to local and global modes in spatially-developing flows. *Phys. Rev. Lett.* **60**, 25–28.

DAVIS, R. W., MOORE, E. F. & PURTELL, L. P. 1983 A numerical–experimental study of confined flow around rectangular cylinders. *Phys. Fluids* **27** (1), 46–59.

DE, A. K. & DALAL, A. 2007 Numerical study of laminar forced convection fluid flow and heat transfer from a triangular cylinder placed in a channel. *J. Heat Transfer* **129**, 646–656.

DELBENDE, I. & CHOMAZ J.-M. 1998 Nonlinear convective/absolute instabilities in parallel two-dimensional wakes. *Phys. Fluids* **10** (11), 2724–2736.

DRAZIN, P. G. & REID, W. H. 1981 *Hydrodynamic Stability*. Cambridge University Press.

HINCH, E. J. 1984 A note on the mechanism of the instability at the interface between two shearing fluids. *J. Fluid Mech.* **144**, 463–465.

HOOPER, A. P. & BOYD, W. G. C. 1983 Shear-flow instability at the interface between two viscous fluids. *J. Fluid Mech.* **128**, 507–528.

HUANG, W. & SLOAN, D. M. 1994 The pseudospectral method for solving differential eigenvalue problems. *J. Comput. Phys.* **113**, 399–409.

HUERRE, P. & MONKEWITZ, P. A. 1990 Local and global instabilities in spatially developing flows. *J. Fluid Mech.* **22**, 473–537.

HWANG, R. R. & YAO, C.-C. 1997 A numerical study of vortex shedding from a square cylinder with ground effect. *J. Fluids Engng* **119**, 512–518.

JUNIPER, M. P. 2006 The effect of confinement on the stability of planar shear flows. *J. Fluid Mech.* **565**, 171–195.

JUNIPER, M. P. 2007 The full impulse response of two-dimensional shear flows and implications for confinement. *J. Fluid Mech.* **590**, 163–185.

JUNIPER, M. P. 2008 The effect of confinement on the stability of non-swirling round jet/wake flows. *J. Fluid Mech.* **605**, 227–252.

JUNIPER, M. P. & CANDEL, S. M. 2003 The stability of ducted compound flows and consequences for the geometry of coaxial injectors. *J. Fluid Mech.* **482**, 257–269.

KIM, D.-H., YANG, K.-S. & SENDA, M. 2004 Large eddy simulation of turbulent flow past a square cylinder confined in a channel. *Comput. Fluids* **33**, 81–96.

KOCH, W. 1985 Local instability characteristics and frequency determination of self-excited wake flows. *J. Sound Vib.* **99**, 53–83.

LESSHAFT, L. & HUERRE, P. 2007 Linear impulse response in hot round jets. *Phys. Fluids* **19**, 024102.

MATHIS, C., PROVANSAL, M. & BOYER, L. 1984 The Bénard-von Kármán instability: an experimental study near the threshold. *J. Phys. (Paris) Lett.* **45**, 483–491.

Meliga, P., Sipp, D. & Chomaz, J.-M. 2008 Absolute instability in axisymmetric wakes: compressible and density variation effects. *J. Fluid Mech.* **600**, 373–401.

Monkewitz, P. A. 1988 The absolute and convective nature of instability in two-dimensional wakes at low Reynolds numbers. *Phys. Fluids* **31**, 999–1006.

Monkewitz, P. A. & Sohn, K. D. 1988 Absolute instability in hot jets. *AIAA J.* **26**, 911–916.

Pier, B. 2002 On the frequency selection of finite-amplitude vortex shedding in the cylinder wake. *J. Fluid Mech.* **458**, 407–417.

Richter, A. & Naudascher, E. 1976 Fluctuating forces on a rigid circular cylinder in confined flow. *J. Fluid Mech.* **78**, 561–576.

Shair, F., Grove, A., Petersen, E. & Acrivos, A. 1963 The effect of confining walls on the stability of the steady wake behind a circular cylinder. *J. Fluid Mech.* **17**, 546–550.

Sreenivasan, K. R., Raghu, S. & Kyle, D. 1989 Absolute instability in variable density round jets. *Exp. Fluids* **7**, 309–317.

Tammisola, O. 2009 Linear stability of plane wakes and liquid jets: global and local approach. Licentiate thesis, KTH, Stockholm.

Turki, S., Abbasi, H. & Nasrallah, S. B. 2003 Effect of the blockage ratio on the flow in a channel with a built-in square cylinder. *Comput. Mech.* **33**, 22–29.

Weideman, J. A. C. & Reddy, S. C. 2000 A MATLAB differentiation matrix suite. *ACM Trans. Math. Software* **26**, 465–519 (http://www.mathworks.com/matlabcentral/fileexchange/).

Yih, C.-S. 1967 Instability due to viscosity stratification. *J. Fluid Mech.* **27**, 337–352.

Yu, M.-H. & Monkewitz, P. A. 1990 The effect of non-uniform density on the absolute instability of planar inertial jets and wakes. *Phys. Fluids* A **2** (7), 1175–1181.

Yu, M.-H. & Monkewitz, P. A. 1993 Oscillations in the near field of a heated two-dimensional jet. *J. Fluid Mech.* **255**, 323–347.